Optics Communications 329 (2014) 44–56

Contents lists available at ScienceDirect

Optics Communications

journal homepage: www.elsevier.com/locate/optcom

High-speed real-time 3-D coordinates measurement based on fringe projection profilometry considering camera lens distortion

Shijie Feng [a,b,*], Qian Chen [a,b], Chao Zuo [a], Jiasong Sun [a], Shi Ling Yu [a]

[a] Jiangsu Key Laboratory of Spectral Imaging & Intelligent Sense, Nanjing University of Science and Technology, Nanjing, Jiangsu Province 210094, China
[b] Key Laboratory of Photoelectronic Imaging Technology and System, Ministry of Education of China. Beijing Institute of Technology, Beijing 100081, China

ARTICLE INFO

Article history:
Received 13 December 2013
Received in revised form
25 April 2014
Accepted 27 April 2014
Available online 13 May 2014

Keywords:
High-speed real-time 3-D measurement
Dynamic scene
Fringe projection
Lens distortion

ABSTRACT

Optical three-dimensional (3-D) profilometry is gaining increasing attention for its simplicity, flexibility, high accuracy, and non-contact nature. Recent advances in imaging sensors and digital projection technology further its progress in high-speed, real-time applications, enabling 3-D shapes reconstruction of moving objects and dynamic scenes. However, the camera lens is never perfect and the lens distortion does influence the accuracy of the measurement result, which is often overlooked in the existing real-time 3-D shape measurement systems. To this end, here we present a novel high-speed real-time 3-D coordinates measuring technique based on fringe projection with the consideration of the camera lens distortion. A pixel mapping relation between a distorted image and a corrected one is pre-determined and stored in computer memory for real-time fringe correction. The out-of-plane height is obtained firstly and the acquisition for the two corresponding in-plane coordinates follows on the basis of the solved height. Besides, a method of lookup table (LUT) is introduced as well for fast data processing. Our experimental results reveal that the measurement error of the in-plane coordinates has been reduced by one order of magnitude and the accuracy of the out-plane coordinate been tripled after the distortions being eliminated. Moreover, owing to the generated LUTs, a 3-D reconstruction speed of 92.34 frames per second can be achieved.

1. Introduction

Three dimensional (3-D) geometric shape measurements have found wide applications in the fields of industrial manufacturing, fast reverse engineering, quality control, biomedical sciences, etc. Compared with the traditional technique that adopts a coordinate measuring machine to retrieve surface contour, the optical 3-D measurement method is non-invasive since no surface contact is required. In addition, its measurement speed is much faster than the conventional point-by-point scanning measurement technique.

Over the years, lots of optical 3-D shape measurement methods have been developed [1]. Among them, fringe projection profilometry has been considered as one of the most reliable techniques due to the advantages of high accuracy, non-scanning property and full-field measurement. Furthermore, with recent advances in digital projection technology, high-speed real-time 3-D measurement techniques based on digital fringe projection are expanding rapidly. These techniques enable a surface to be reconstructed in a very short time period, thus will be of great potential for some time-critical applications, e.g. biomedical dynamic 3-D imaging, deformation analysis under stress and vehicle collision research.

Traditionally, fringe projection based high-speed real-time 3-D shape measurement methods can be classified into two categories: the first one is to project a single pattern to inspect an object of interest [2–4]. Although this strategy is insensitive to object motion, it has disadvantages that the phase calculation relies on the spatial neighborhood phase distribution, which reduces the phase resolution and cannot recover discontinuous surfaces. The second one is to project multiple phase-shifted fringe patterns [5–7]. As the phase is calculated according to the captured intensities of several phase-shifted images at the same pixel, this strategy offers higher measurement accuracy and spatial resolution than the single pattern method. Further, it is more robust since it is less sensitive to ambient light and object surface reflectivity. Although this method may be susceptible to the object movement, the associated side effects can be reduced to the minimum as long as the projector/camera pair runs fast enough. Exploiting this strategy, Zhang et al. developed a real-time 3-D shape measurement system using graphics processing unit to accomplish complex computations such as arctangent function and 3-D coordinates calculations [8]. For the image of 532×500, their system allows 3-D coordinates measurement at 25.56 frames per second. Besides, Liu et al. reported a dual-frequency pattern

* Corresponding author at: Jiangsu Key Laboratory of Spectral Imaging & Intelligent Sense, Nanjing University of Science and Technology, Nanjing, Jiangsu Province 210094, China.
E-mail address: geniusshijie@163.com (S. Feng).

http://dx.doi.org/10.1016/j.optcom.2014.04.067
0030-4018/

scheme [9] in which several LUTs are created to compute the phase map, modulation map, and coordinates, hugely lowering the computational complexity and enabling the shape reconstruction in less than ten milliseconds. Also, Zuo et al. developed a system [10] using a modified low cost commodity DLP projector that is able to work at 360 Hz and proposed a four patterns projection strategy to recover the absolute phase map, achieving a dynamic scene measurement at 120 frames per second.

From the previous works above, we find that the camera lens distortion is rarely taken into account in the high-speed real-time 3-D shape measurement. In experiments, however, the lens distortion does affect the measurement accuracy and in most cases it cannot be simply neglected, especially for some low cost systems where the optics involved are of relatively poor imaging quality in general. In a traditional 3-D measurement system where the processing time is not a key factor, the correction of camera lens distortion can be performed directly. However, for time-critical high-speed applications, the time-consuming correction algorithm is no longer appropriate to be performed directly during the real-time process. Therefore, there is an urgent need for a method that is capable of realizing high-speed real-time distortion-free 3-D geometric shape measurement. The goal of this paper is to propose a new high-speed real-time 3-D coordinates measuring approach that eliminates the influence of the camera lens distortion. In this research, we firstly calibrate the used camera and every captured fringe image is processed with distortion correction before phase retrieval. To reduce the time cost in terms of the distortion correction, a pixel correspondence between the distorted and the undistorted images is pre-computed and will be directly used for correction in the real-time process. Then, our previously presented five fringe patterns strategy [11] is introduced to calculate the absolute phase map with the purpose of making the proposed approach less sensitive to object motion. As for the 3-D coordinates acquisition, the out-of-plane height is obtained firstly by the technique in Ref. [12] and the corresponding two in-plane coordinates are solved according to the calculated height, together with the calibrated intrinsic and extrinsic parameters of the camera. In addition, several LUTs are established for the computations of the phase map and 3-D coordinates so as to lower the computational complexity and enhance the measurement speed. The experimental results verify the validity of the proposed method.

2. Phase retrieval

Phase-shifting algorithm is one of the most commonly used techniques for phase recovery due to its high accuracy and insensitivity to ambient illumination. For traditional N-step phase-shifting algorithm, the three-step phase-shifting strategy has been extensively adopted in high-speed applications because it only requires three phase-shifting images to obtain a full-field phase map. The obtained phase map by the phase-shifting algorithm is wrapped and it needs to be unwrapped before applying to 3-D reconstruction. Practically, the temporal phase unwrapping algorithm is often used to eliminate the phase ambiguity. However, as to the conventional temporal phase unwrapping algorithm, it will ask for another set of N fringe patterns with a different stripe frequency if the wrapped phase is calculated by a N-step phase-shifting algorithm. Therefore, at least six fringe patterns are required to obtain a continuous absolute phase map by the traditional method.

In our previous study [11], we have proposed a bi-frequency phase-shifting method. As it only exploits five fringe images to compute an absolute phase map, it will be less susceptible to the movement of object compared with the traditional method when measuring a dynamic scenario. In the five fringe images, three of them are of high-frequency and can be expressed as

$$I_1(x,y) = I'(x,y) + I''(x,y)\cos(\phi_h(x,y) - 2\pi/3), \tag{1}$$

$$I_2(x,y) = I'(x,y) + I''(x,y)\cos(\phi_h(x,y)), \tag{2}$$

$$I_3(x,y) = I'(x,y) + I''(x,y)\cos(\phi_h(x,y) + 2\pi/3), \tag{3}$$

where $I'(x,y)$ is the average intensity, $I''(x,y)$ being the intensity modulation and $\phi_h(x,y)$ the phase to be solved from the high-frequency fringe images. $I'(x,y)$ and $\phi_h(x,y)$ can then be computed by the following equations:

$$I'(x,y) = \frac{I_1(x,y) + I_2(x,y) + I_3(x,y)}{3}, \tag{4}$$

$$\phi_h(x,y) = \tan^{-1}\frac{\sqrt{3}(I_1(x,y) - I_3(x,y))}{2I_2(x,y) - I_1(x,y) - I_3(x,y)}. \tag{5}$$

The rest two fringe images are of low-frequency and written as

$$I_4(x,y) = I'(x,y) + I''(x,y)\sin(\phi_l(x,y)), \tag{6}$$

$$I_5(x,y) = I'(x,y) + I''(x,y)\cos(\phi_l(x,y)), \tag{7}$$

where $\phi_l(x,y)$ is the phase relating to the low-frequency fringe images and can be obtained by

$$\phi_l(x,y) = \tan^{-1}\frac{I_4(x,y) - I'(x,y)}{I_5(x,y) - I'(x,y)} \tag{8}$$

Finally, the absolute phase map $\Phi(x,y)$ can be solved by

$$\Phi(x,y) = \phi_h(x,y) + 2\pi Round\left(\frac{k\phi_l(x,y) - \phi_h(x,y)}{2\pi}\right) \tag{9}$$

Here the *Round* represents a function to get the nearest integer. The coefficient k needs to satisfy $\lambda_l = k\lambda_h$, where λ_h denotes the wavelength of the high-frequency patterns and λ_l the wavelength of the low-frequency fringe. Assume that the used projector has a resolution of $W \times H$ and the projected fringe patterns are vertical, we take $\lambda_l = W$ [13,14]. By this way, the phase map of ϕ_l solved by Eq. (8) is continuous, which means the ϕ_l needs not to be unwrapped and can be substituted directly into Eq. (9) for the absolute phase calculation.

3. Camera model and phase to 3-D coordinates conversion

Generally, the pinhole model is used to describe a camera with its intrinsic and extrinsic parameters. Fig. 1 illustrates a linear camera model where $O_w - X_wY_wZ_w$ represents the world coordinate system that is the base reference system for all objects involved, and $O_c - X_cY_cZ_c$ the camera coordinate system whose origin coincides with the center of the camera. The image plane at the position of $z_c = f$ corresponds to the CCD sensor array and is parallel to plane $X_cO_cY_c$, where f is the focal length of the camera. A virtual normalized plane is created parallel to the image plane and located at $z_c = 1$. An arbitrary point P with coordinate $[x_w, y_w, z_w]^T$ in the world coordinate system can be transformed into $[x_c, y_c, z_c]^T$ in the camera coordinate system by the following equation:

$$\begin{bmatrix} x_c \\ y_c \\ z_c \end{bmatrix} = [R, T]\begin{bmatrix} x_w \\ y_w \\ z_w \end{bmatrix} = \begin{bmatrix} r_{11} & r_{12} & r_{13} & t_1 \\ r_{21} & r_{22} & r_{23} & t_2 \\ r_{31} & r_{32} & r_{33} & t_3 \end{bmatrix}\begin{bmatrix} x_w \\ y_w \\ z_w \end{bmatrix}, \tag{10}$$

where $R = [r_{ij}]$ $(i,j = 1,2,3)$ represents the rotation matrix and $T = [t_1, t_2, t_3]^T$ the translation vector. Then the projective point p_n

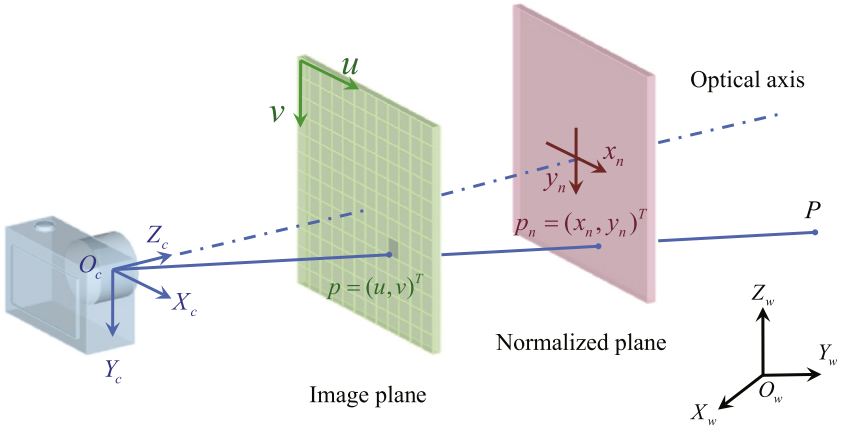

Fig. 1. The linear camera model.

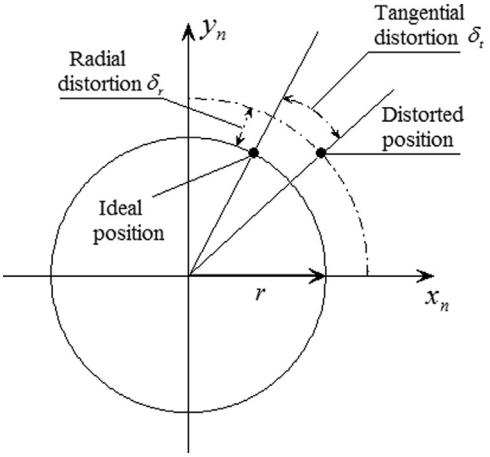

Fig. 2. Camera lens distortion.

on the normalized plane can be given by

$$p_n = \begin{bmatrix} x_n \\ y_n \end{bmatrix} = \begin{bmatrix} x_c/z_c \\ y_c/z_c \end{bmatrix}. \tag{11}$$

And, the image point p can be expressed as

$$p = \begin{bmatrix} u \\ v \end{bmatrix} = \begin{bmatrix} x_n f_u + u_0 \\ y_n f_v + v_0 \end{bmatrix}, \tag{12}$$

where f_u and f_v represent the horizontal and vertical focal length respectively. And u_0 and v_0 describe the location of the principal point on the image plane. Combine Eqs. (10)–(12), gives

$$\begin{cases} \frac{r_{11}x_w + r_{12}y_w + r_{13}z_w + t_1}{r_{31}x_w + r_{32}y_w + r_{33}z_w + t_3} = x_n = \frac{u - u_0}{f_u} \\ \frac{r_{21}x_w + r_{22}y_w + r_{23}z_w + t_2}{r_{31}x_w + r_{32}y_w + r_{33}z_w + t_3} = y_n = \frac{v - v_0}{f_v} \end{cases}. \tag{13}$$

Actually, this linear camera model mentioned above is an ideal model which does not take into account of the destructive effects of the camera lens distortion [15]. In this paper, we focus on two dominating types of lens distortion, the radial distortion and the tangential distortion which are shown in Fig. 2. It should be noted that normally the radial and tangential distortions high to fourth order would be adequate for practical application [16].

The radial distortion δ_r, which is mainly caused by the defective curve of the lens components, is radially symmetric about the optical axis and can be classified as either pincushion distortion or barrel distortion. This kind of distortion can be written as

$$\delta_r = (k_1 {r_n}^2 + k_2 {r_n}^4) p_n = \begin{bmatrix} (k_1 {r_n}^2 + k_2 {r_n}^4) x_n \\ (k_1 {r_n}^2 + k_2 {r_n}^4) y_n \end{bmatrix}, \tag{14}$$

where k_1 and k_2 are the radial distortion coefficients, and ${r_n}^2 = {x_n}^2 + {y_n}^2$. Then the tangential distortion δ_t may arise when the optical centers of the lens surfaces are not strictly collinear and it can be expressed as

$$\delta_t = \begin{bmatrix} 2k_3 x_n y_n + k_4(2x_n^2 + r_n^2) \\ k_3(2y_n^2 + r_n^2) + 2k_4 x_n y_n \end{bmatrix}, \tag{15}$$

where k_3 and k_4 are the tangential distortion coefficients. Next, combine Eqs. (14) and (15), the distorted point $[x_d, y_d]^T$ on the normalized plane can be determined by

$$\begin{bmatrix} x_d \\ y_d \end{bmatrix} = p_n + \delta_r + \delta_t = \begin{bmatrix} x_n(1 + k_1 {r_n}^2 + k_2 {r_n}^4) + 2k_3 x_n y_n + k_4(2x_n^2 + r_n^2) \\ y_n(1 + k_1 {r_n}^2 + k_2 {r_n}^4) + k_3(2y_n^2 + r_n^2) + 2k_4 x_n y_n \end{bmatrix}. \tag{16}$$

And as the result of the distortion, the Eq. (12) can be rewritten as

$$p_d = \begin{bmatrix} u_d \\ v_d \end{bmatrix} = \begin{bmatrix} x_d f_u + u_0 \\ y_d f_v + v_0 \end{bmatrix}, \tag{17}$$

where p_d denotes the distorted image point on the image plane.

Due to the effect of lens distortion, most pixels are influenced to some extent. The impact is insignificant if the pixels locate around the principal point on the image plane, however it will be much more evident when the pixels locate relatively far away from the principal point, particularly near the border of the image. In cases where the lens distortion is not taken into account, the solved $[x_n, y_n]^T$ is actually the $[x_d, y_d]^T$, thus leading to incorrect 3-D coordinates retrieval.

Therefore, to correct lens distortion, *img_rect* is used to represent the corrected image and *img_distort* the distorted image, the distortion can be eliminated by the following equation:

$$img\_rect(u, v) = img\_dist(u_d, v_d), \tag{18}$$

where

$$\begin{cases} u_d = [x_n(1 + k_1 {r_n}^2 + k_2 {r_n}^4) + 2k_3 x_n y_n + k_4(2x_n^2 + r_n^2)] f_u + u_0 \\ v_d = [y_n(1 + k_1 {r_n}^2 + k_2 {r_n}^4) + k_3(2y_n^2 + r_n^2) + 2k_4 x_n y_n] f_v + v_0 \end{cases},$$

$$\begin{cases} x_n = \frac{u - u_0}{f_u} \\ y_n = \frac{v - v_0}{f_v} \end{cases} \quad and \quad {r_n}^2 = {x_n}^2 + {y_n}^2.$$

It should be noted that the calculated coordinates u_d and v_d may not be proper to be directly substituted into Eq. (18) since

they may not be integers in general. To solve this issue, bilinear interpolation algorithm is introduced into our research and its schematic diagram is shown in Fig. 3. Thus, by the bilinear interpolation we will have

$$\begin{aligned} img\_dist(u_d,v_d) = {} & img\_dist(u_1,v_1)(u_2-u_d)(v_2-v_d) \\ & + img\_dist(u_2,v_1)(u_d-u_1)(v_2-v_d) \\ & + img\_dist(u_1,v_2)(u_2-u_d)(v_d-v_1) \\ & + img\_dist(u_2,v_2)(u_d-u_1)(v_d-v_1), \end{aligned} \tag{19}$$

where u_1 and v_1 are the nearest integers to u_d and v_d while smaller than u_d and v_d. And u_2 and v_2 are the nearest integers that are larger than u_d and v_d.

As to the correction algorithm, it is not hard to find that the computational complexity of Eq. (18) is not low, which is one major obstacle for the real-time implementation of our method. Thus to handle this issue, Eq. (18) expressing the pixel mapping relationship between the distorted and the corrected image is performed and stored in computer memory prior to the real-time measurement since the pixel positions before and after distortion correction, intrinsic parameters and distortion coefficients are all known once the camera is calibrated. As the time-costing mapping function is pre-determined, Eq. (19) can be carried out in real-time process to generate an undistorted image because of its low computational complexity.

After correcting the image distortion, we direct our attention to the 3-D coordinates retrieval. From Eq. (13), we find that this equation builds a relationship between a random point in world coordinate system and its projection on the image plane. But it can be found that there only exist two equations which are not enough to obtain the 3-Dcoordinates (x_w, y_w, z_w) composed of three independent components. Therefore to cope with this issue, we determine the coordinate z_w firstly and then retrieve the in-plane coordinates (x_w, y_w) with the known z_w for each point.

The technique using a governing equation to calculate surface height relative to a reference plane is commonly adopted for the reason that it does not require precise determination for the geometrical parameters, such as the distance between the camera and the projector, and the capture or projection orientation. This means the camera and the projector can be arbitrarily arranged as long as the range of projection within the field of view of the camera. In this research, we place the world coordinate system $(O_w - X_w Y_w Z_w)$ on the reference plane and thus the obtained out-of-plane height can serve as coordinate z_w. A governing equation [12] can be expressed as

$$z_w = \frac{1 + c_1\Phi + (c_2 + c_3\Phi)u + (c_4 + c_5\Phi)v + (c_6 + c_7\Phi)u^2 + (c_8 + c_9\Phi)v^2 + (c_{10} + c_{11}\Phi)uv}{d_0 + d_1\Phi + (d_2 + d_3\Phi)u + (d_4 + d_5\Phi)v + (d_6 + d_7\Phi)u^2 + (d_8 + d_9\Phi)v^2 + (d_{10} + d_{11}\Phi)uv}, \tag{20}$$

where c_1–c_{11} and d_0–d_{11} are coefficients to be estimated, and Φ being the calculated absolute phase acquired by Eq. (9). All of the coefficients can be determined by exploiting a least-squares inverse algorithm with a reference plane (z_w=0) and at least two gauge blocks of different heights which are precisely known in advance. The least-squares error can be written as

$$E = \sum_{n=1}^{m} (z_n - z'_n)^2, \tag{21}$$

where z_n denotes the calculated height of the nth data point by using Eq. (20), z'_n being the actual height of the nth point, and m the total number of the data points used for the coefficient estimation. Generally, the more data points are selected, the more accurate result can be obtained.

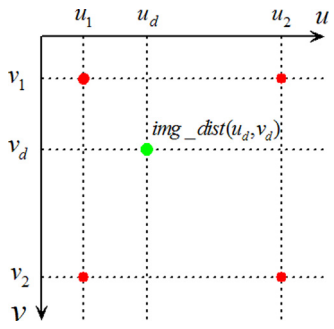

Fig. 3. Schematic diagram of bilinear interpolation.

Traditionally, to calibrate the measurement system accurately, gauge blocks of different sizes should be employed. However, the manufacturing of a mass of gauge blocks with high precision would be an extremely costly work. Therefore, to circumvent this issue, we develop an alternative approach without using multiple gauge blocks. Firstly we set a basic position for a calibration board as the reference plane and then make the board move along its normal direction which is shown in Fig. 4. Every time the calibration board forwards a fixed step and data points are selected on the surface of the calibration board at each position. The total number of the movements will largely rely on the height (depth) range of the measured object. Since the step size and the number of shifts can be set based on the actual requirement, this approach would be more flexible and practical than the strategy with use of gauge blocks. As soon as the out-of-plane coordinate z_w is calculated, the corresponding in-plane coordinates x_w and y_w can be uniquely solved by Eq. (13). However, it should be noted that the calculations for the 3-D coordinates may be inappropriate to be directly applied in the high-speed measuring process as the computational complexity of the Eqs. (5), (8), (13) and (20) is still relatively high at this moment. Hence, in the coming section, a fast data processing algorithm is introduced.

4. LUT based fast and lossless data processing technique

LUT based approaches are extensively adopted in applications where the minimum processing time is highly desirable. As all of the values of interest are pre-calculated and stored in computer memory in advance, they can be accessed directly by a simple indexing operation without the need to conduct complex arithmetical operations, thus saving a large amount of time. In this paper, several lossless LUTs have been created for solving the phase maps of ϕ_h and ϕ_l, and the 3-D coordinate (x_w, y_w, z_w).

4.1. LUTs for phase calculation

To calculate the phase, two LUTs are built for Eqs. (5) and (8) respectively

$$\phi_h\_LUT[I,J] = \tan^{-1}\left(\frac{\sqrt{3}I}{J}\right) \quad and \quad \begin{cases} I = I_1 - I_3 \\ J = 2I_2 - I_1 - I_3 \end{cases}, \tag{22}$$

$$\phi_l\_LUT[I,J] = \tan^{-1}\left(\frac{I}{J}\right) \quad and \quad \begin{cases} I = I_4 - \frac{1}{3}(I_1 + I_2 + I_3) \\ J = I_5 - \frac{1}{3}(I_1 + I_2 + I_3) \end{cases}. \tag{23}$$

These two LUTs can accurately cover the whole variation range of ϕ_h and ϕ_l, since the captured intensity at each pixel is represented by an integer which varies from 0 to 255 if 8 bits are used to store the intensity value.

4.2. LUTs for 3-D coordinates retrieval

As mentioned in the previous section, the out-of-plane coordinate z_w needs to be determined firstly before acquiring the in-plane coordinates x_w and y_w. Thus, rearranging Eq. (20) gives

$$z_w(u,v)=\frac{\Phi(u,v)(c_1+c_3u+c_5v+c_7u^2+c_9v^2+c_{11}uv)+1+c_2u+c_4v+c_6u^2+c_8v^2+c_{10}uv}{\Phi(u,v)(d_1+d_3u+d_5v+d_7u^2+d_9v^2+d_{11}uv)+d_0+d_2u+d_4v+d_6u^2+d_8v^2+d_{10}uv}, \tag{24}$$

where (u,v) is the pixel coordinate on the image plane. Then, four LUTs are built for Eq. (24) and we have

$$z_w(u,v)=\frac{\Phi(u,v)Z1\_LUT[u,v]+Z2\_LUT[u,v]}{\Phi(u,v)Z3\_LUT[u,v]+Z4\_LUT[u,v]}, \tag{25}$$

$$Z1\_LUT[u,v]=c_1+c_3u+c_5v+c_7u^2+c_9v^2+c_{11}uv, \tag{26a}$$

$$Z2\_LUT[u,v]=1+c_2u+c_4v+c_6u^2+c_8v^2+c_{10}uv, \tag{26b}$$

$$Z3\_LUT[u,v]=d_1+d_3u+d_5v+d_7u^2+d_9v^2+d_{11}uv, \tag{26c}$$

$$Z4\_LUT[u,v]=d_0+d_2u+d_4v+d_6u^2+d_8v^2+d_{10}uv\cdot \tag{26d}$$

Substituting Eq. (25) into Eq. (13), x_w and y_w can be obtained respectively by

$$x_w(u,v)=X1\_LUT[u,v]+X2\_LUT[u,v]z_w(u,v), \tag{27}$$

$$y_w(u,v)=Y1\_LUT[u,v]+Y2\_LUT[u,v]z_w(u,v), \tag{28}$$

where $X1\_LUT$, $X2\_LUT$, $Y1\_LUT$, $Y2\_LUT$ are defined in the Appendix. Since u and v represent the image column and row respectively, the size of the created LUTs to calculate the 3-D coordinates will depend on the resolution of the used camera. Compared with solving Eqs. (20) and (13) directly, it can be found that the proposed LUT based data processing technique is able to yield lossless 3-D coordinates merely by 4 multiplications, 4 additions and 1 division, thus will greatly reduce the time cost.

5. Experiments

To testify the proposed method, we employed our high-speed real-time 3-D measurement system [17] composed of a high-speed black and white CCD camera, a modified off-the-shelf DLP projector and a personal computer. A Field-Programmable Gate Array (FPGA) board is integrated into our system to synchronize the camera and projector making them run at a rate of 120 frames per second. Before experiments, the nonlinearity of the projector was corrected to ensure high measurement accuracy. To reduce the random noise resulted from short exposure time, 3×3 Gaussian filter was used to smooth the captured image.

5.1. Camera calibration and determination for governing equation coefficients

The used camera was calibrated by the Matlab calibration toolbox [16] exploiting a black and white calibration board whose pattern is formed by 99 white circles in 11 columns and 9 rows. And the distance between the center of each circles is 30 mm. We captured 20 images of the calibration board with different positions and orientations as shown in Fig. 5(a). The plane of the calibration board in the first calibration image was chosen as the reference plane and the world

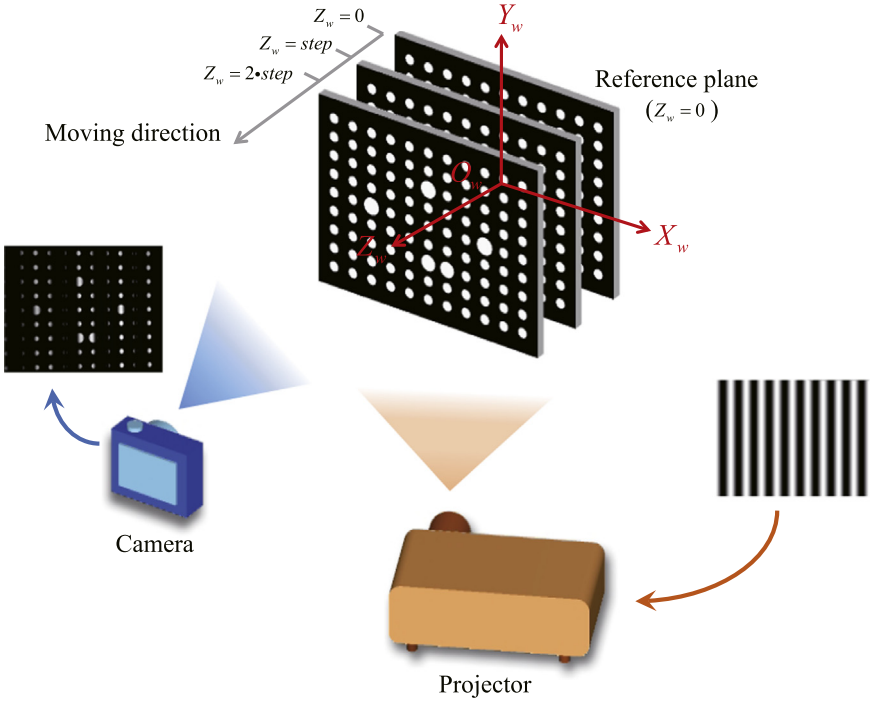

Fig. 4. Calibration process for the unknown coefficients in governing equation.

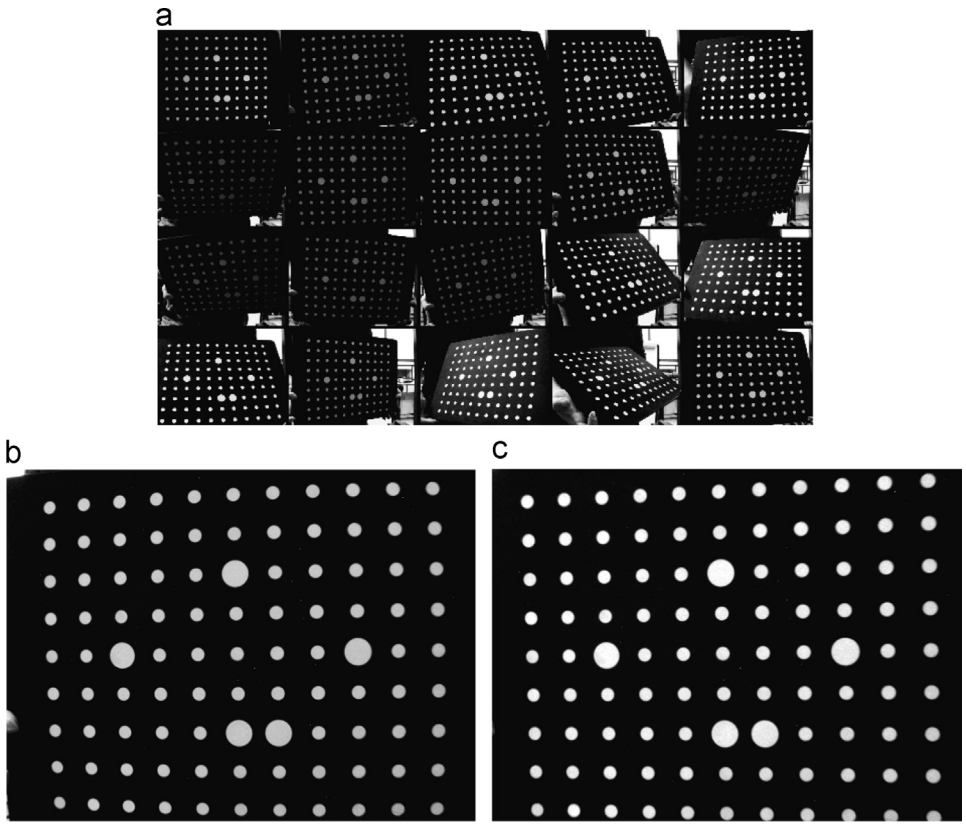

Fig. 5. Camera calibration. (a) 20 images being used for calibration; (b) A distorted image and (c) Its undistorted image.

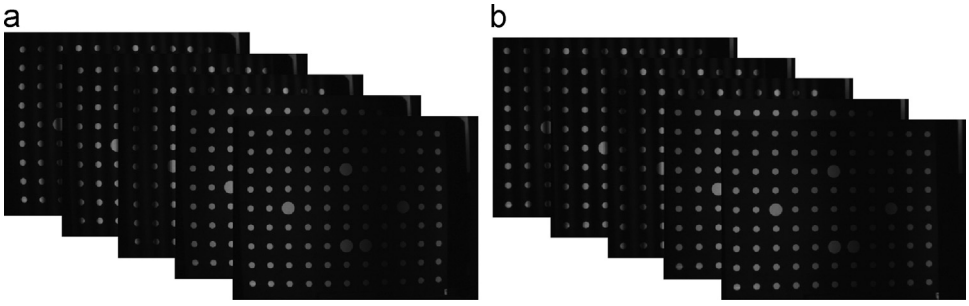

Fig. 6. Fringe images for testing the accuracy of in-plane coordinates. (a) Primitive fringe images used by the method neglecting lens distortion and (b) corrected fringe images utilized in the proposed method.

coordinate system was set at the center of the calibration board. The intrinsic parameters matrix of the camera is as follows:

$$A=\begin{bmatrix} f_u & 0 & u_0 \\ 0 & f_v & v_0 \\ 0 & 0 & 1 \end{bmatrix}=\begin{bmatrix} 914.57096 & 0 & 317.66185 \\ 0 & 915.09352 & 227.26700 \\ 0 & 0 & 1 \end{bmatrix}\cdot$$

The calculated distortion coefficients high to fourth order is shown in matrix Kc,

$$Kc=[k_1,k_2,k_3,k_4]=[-0.32944,0.20982,0.00179,-0.00152]\cdot$$

And the extrinsic parameters matrix which was calculated according to the first calibration image is

$$[R\quad T]=\begin{bmatrix} 0.997387 & -0.00915 & 0.071662 & -13.7401 \\ -0.00896 & -0.99996 & -0.00302 & 7.128341 \\ 0.071687 & 0.002374 & -0.99742 & 544.6543 \end{bmatrix}\cdot$$

To see the effect of lens distortion clearly, two images of the calibration board before and after the distortion correction are illustrated in Fig. 5(b) and (c) respectively. By comparison, it is obvious to see that the circles near the border of the calibration board have been rearranged in a slight arc due to the effect of the lens distortion.

After the camera calibration, we computed the coefficients in Eq. (20). To precisely control the moving step, the calibration board was placed on a motorized translation stage with displacement precision of 1 μm and the normal direction of the calibration board was coaxial with the moving direction of the translation stage. The step in Fig. 4 was set to be 3 mm. Totally, the whole moving distance of the calibration board was 99 mm with regard to the reference plane. At each position, images of the calibration board with projected fringes were used for phase retrieval after they had been undistorted. And then the data points were selected within the white circles of the calibration board. By using the Levenberg–Marquardt method, the determined coefficients are

$$c_1\text{–}c_{11}=[-255038148.19393,\ 36853211.89023,\ 269362.36249,$$
$$-1310316.72298,\ -451.38022,\ -29665.76779,$$
$$-53.37696,\ 680.91566,\ -6.35272,\ 1675.93245,\ 0.02991],$$

$$d_0 - d_{11} = [20915440.79027,\ -288325.98495,\ 48700.96983,\ 319.29858,\ -304.83788,\ -15.33277,\ -50.53371,\ -0.08833,\ 0.28800,\ 0.00999,\ -0.32732,\ 0.03457]\cdot$$

5.2. Static scene measurements

To evaluate the accuracy of the propose approach, experiments measuring motionless gauge objects have been conducted. The first one was designed for testing the accuracy of the calculated in-plane coordinates (x_w and y_w). With this purpose, a calibration board was measured at the position of the reference plane. For comparison, a measurement without removing the lens distortion was also conducted. Fig. 6(a) illustrates five fringe images without distortion elimination. And Fig. 7(a) shows the corresponding reconstructed 3-D point cloud map viewed from the positive direction of Z_w, in which it is obvious to see that the circles at the left bottom have been shifted by a small amount due to the lens distortion. In contrast, another set of five fringe images, which were processed by Eqs. (18) and (19) for the distortion removal, are shown in Fig. 6(b). The corresponding point cloud map was obtained as Fig. 7(b). It can be seen that those misplaced circles have been moved back to correct positions once the distortion was eliminated.

Four centers of the circles located at four corners of the calibration board were selected and labeled from A to D. The result of measured distances of the four line segments between the chosen centers is illustrated in Table 1. It shows that using the proposed method the measurement accuracy of each segment has been greatly improved. After the distortion correction, the largest error is 0.13 mm which is much less than the smallest error 5.59 mm acquired from the method without distortion correction.

For further accuracy analysis, comparisons between the actual positions of centers of all the circles on the calibration board and their measured results has been conducted since the distance between each center of the circles was known to be 30 mm and the origin of the world coordinate system has been placed at the center of the calibration board. Fig. 8(a) and (b) shows the measurement error distributions of the method without distortion correction and the one with the correction respectively. Each asterisk represents a center of a circle on the calibration board, and the horizontal axis and vertical axis indicate the measurement errors in directions of X_w and Y_w respectively. With the developed approach, the errors in the two directions are cut down to less than 0.2 mm that is an accuracy improvement of one order of magnitude compared with the performance of the counterpart method. Moreover, we calculated the distances from the center of the central circle to the ones of the surrounding circles for the comparison to the true distances. Fig. 8(c) shows the result from the method without distortion correction. It is noted that as the distribution of circles on the calibration board is centrosymmetric, the same distance may correspond to different circles. Thus, each measured distance showed by the dot is the average for those circles. For quantitative comparison, the results of three different distances were displayed. It can be seen that as the distance is farther the measurement error increases and the precision is deteriorated, indicated by the gradually increasing distinction between the measured mean value and the true distance and the larger value of the standard deviation (STD). By contrast, Fig. 8(d) demonstrates the result of the proposed method. It can be found that the curve of the measured data coincident well with the true data for all distances no matter how far it is. The difference between the measured mean value and the true value for the farthest circles is 0.06 mm and the corresponding STD is 0.0492 mm, which have been greatly reduced compared to the results obtained without the distortion correction.

The next experiment was carried out to evaluate the measurement accuracy for coordinate z_w (out-of-plane height). Again, an experiment using the method without distortion correction was conducted for comparison. Two gauge blocks with heights of 50.48 mm and 80.71 mm were inspected and placed against the reference plane. Fig. 9(b) shows the captured five fringe images, in which the effect of distortion was removed by Eqs. (18) and (19), and Fig. 9(a) shows the primitive distorted fringe images. After solving

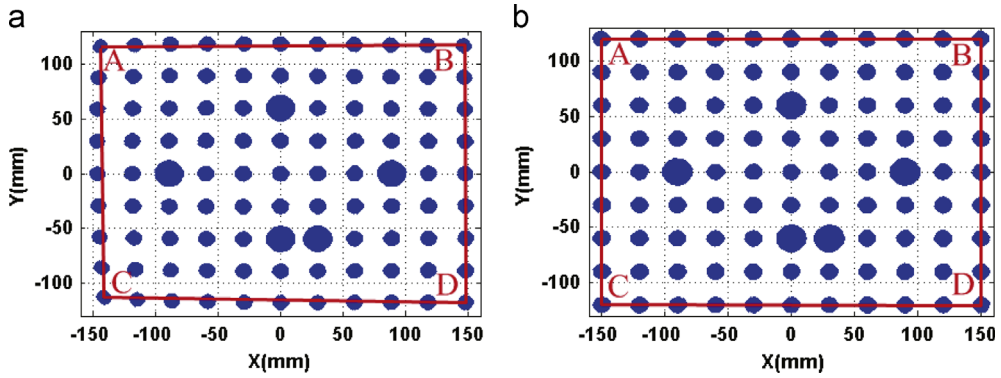

Fig. 7. The solved 3-D point cloud maps viewed from the positive direction of Z_w. (a) The result from method without distortion correction and (b) the result from the proposed method.

Table 1
Measurement results of the four segments.

	Method without distortion correction				Proposed method with distortion correction			
Segments	AB	BD	CD	AC	AB	BD	CD	AC
Measured distance (*mm*)	290.69	234.41	288.98	228.74	299.89	240.13	300.10	239.93
Actual distance (*mm*)	300.01	240.00	300.01	240.02	300.01	240.00	300.01	240.02
Error (*mm*)	9.32	5.59	11.03	11.28	0.12	−0.13	−0.09	0.09

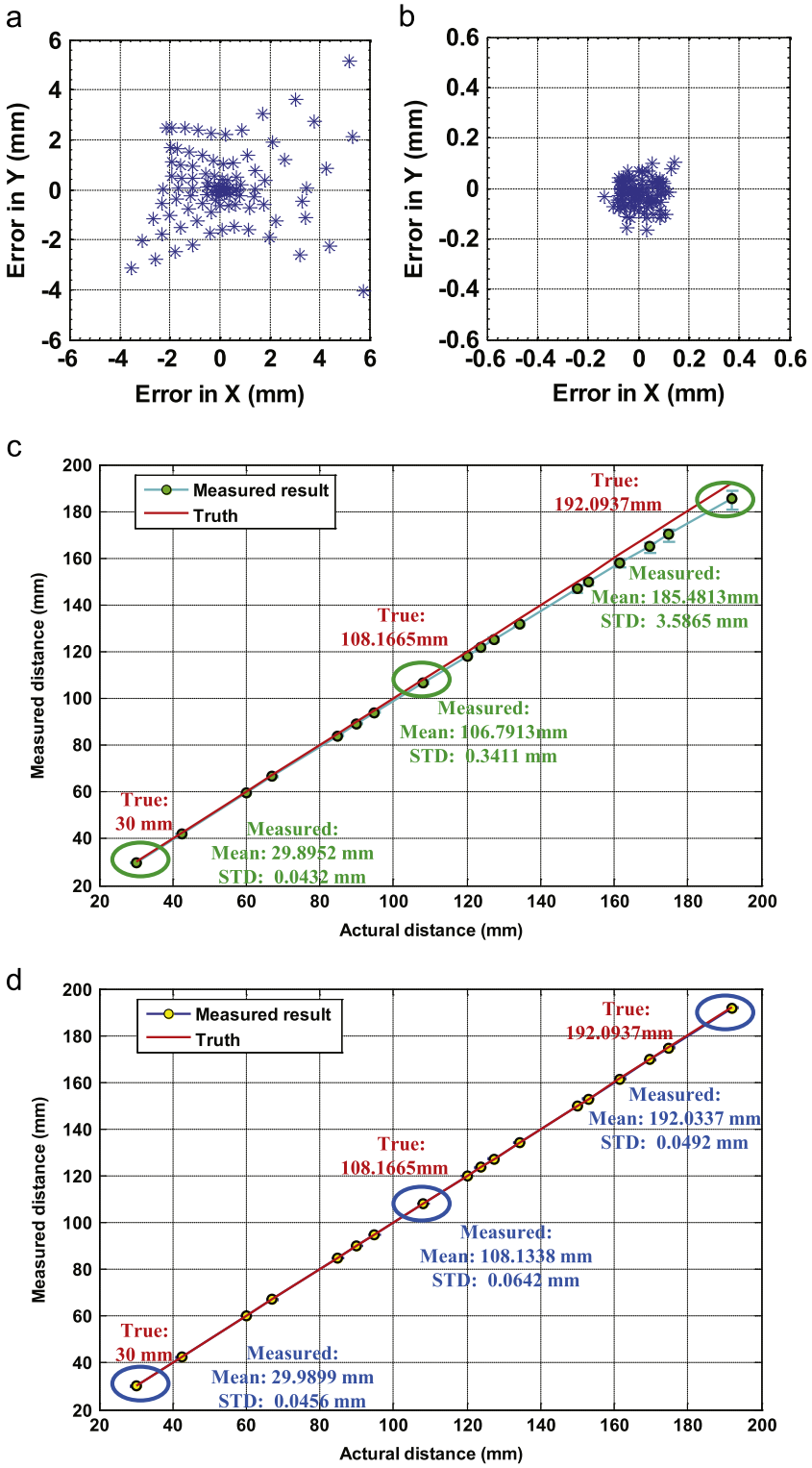

Fig. 8. Measurement errors of the in-plane coordinates. (a) The measurement error in directions of X_w and Y_w when the lens distortion is not considered, (b) the measurement error in directions of X_w and Y_w when the presented method is used, (c) the measured distances between the central circle to the rest circles when the lens distortion is not considered and (d) the measured distances between the central circle to the rest circles when the presented method is used.

the absolute phase map by Eq. (9), the surface heights of the blocks were obtained by Eq. (20). The 3-D reconstruction results are shown in Fig. 10, where (a) illustrates the 3-D model acquired by the method without the distortion correction and (b) shows the one by the proposed method. Since these results look alike in this macroscopic view. A more subtle analysis of the surfaces is shown in Fig. 11. Fig. 11(a) and (b) depicts the blocks surfaces calculated without the elimination of distortion, and Fig. 11(c) and (d) illustrates the ones calculated through the proposed method. Comparing these results, the height distributions of the presented method are more uniform while by the counterpart method the reconstructed planes are undulating. The experimental results show that when neglecting

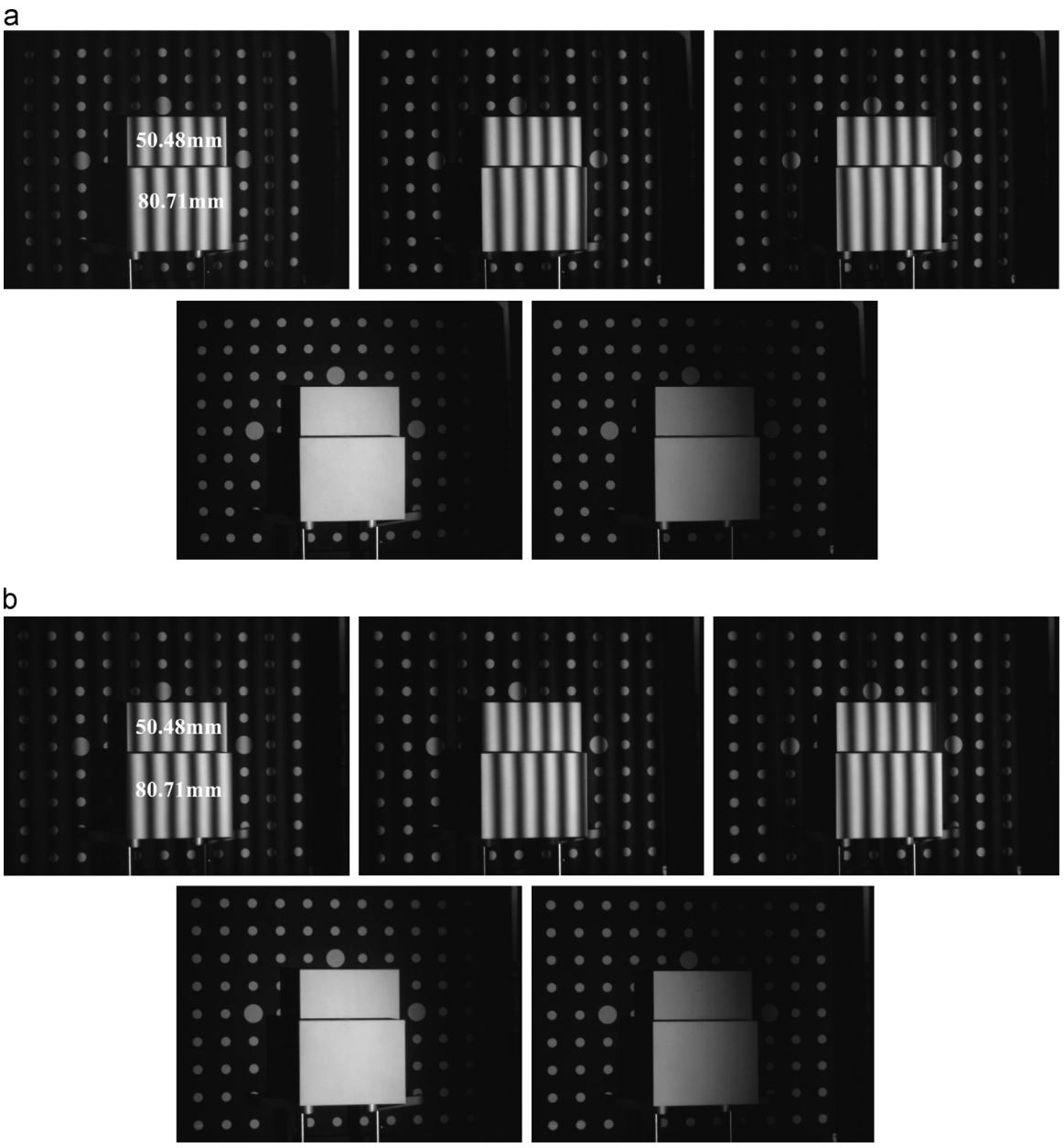

Fig. 9. Fringe images to calculate the out-of-plane heights of the two gauge blocks. (a) Primitive images without distortion rectification and (b) images after the distortion elimination.

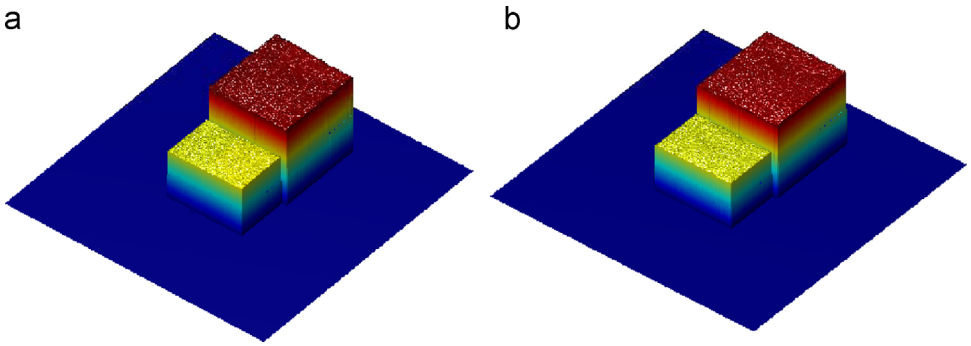

Fig. 10. 3-D reconstruction results. (a) The 3-D model solved without considering camera lens distortion; (b) The 3-D model obtained through the proposed method.

lens distortion the average measured heights of the two blocks are 49.69 mm and 80.94 mm with root mean square (RMS) of 0.836 mm and 0.487 mm, and once the distortion was removed the calculated average heights are 50.56 mm and 80.83 mm with RMS of 0.196 mm and 0.127 mm. It can be found that the measurement accuracy has been tripled by our approach.

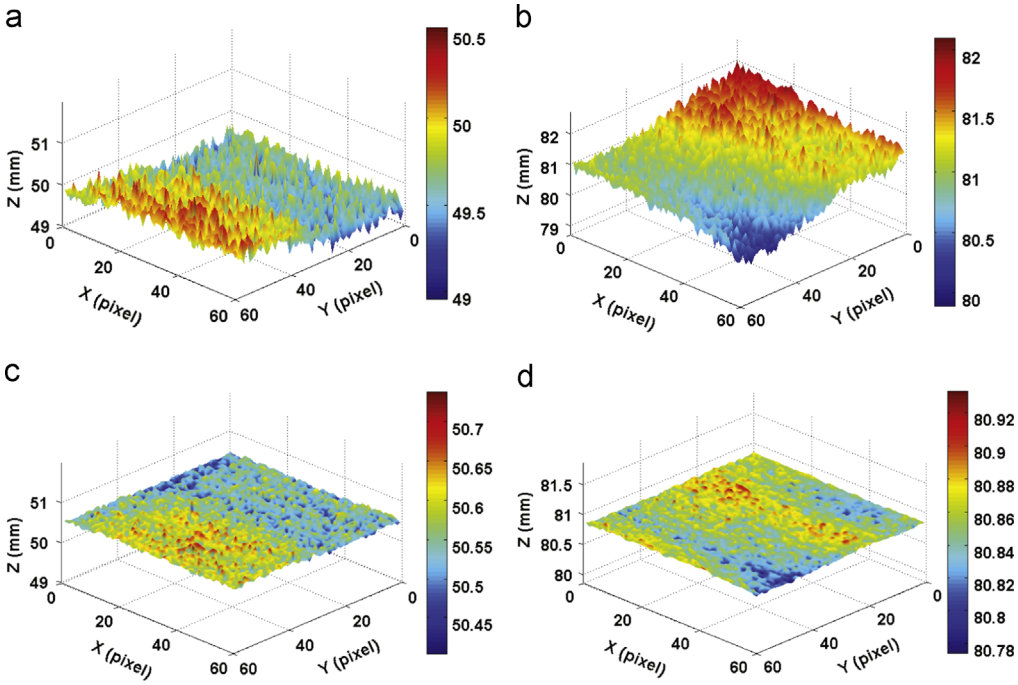

Fig. 11. The surface detail of the reconstructed models. (a) The measured surface of gauge block with height of 50.48 mm when neglecting the lens distortion; (b) The measured surface of gauge block with height of 80.71 mm when neglecting the lens distortion; (c) The measured surface of gauge block with height of 50.48 mm when using the proposed method; (d) The measured surface of gauge block with height of 80.71 mm when using the proposed method.

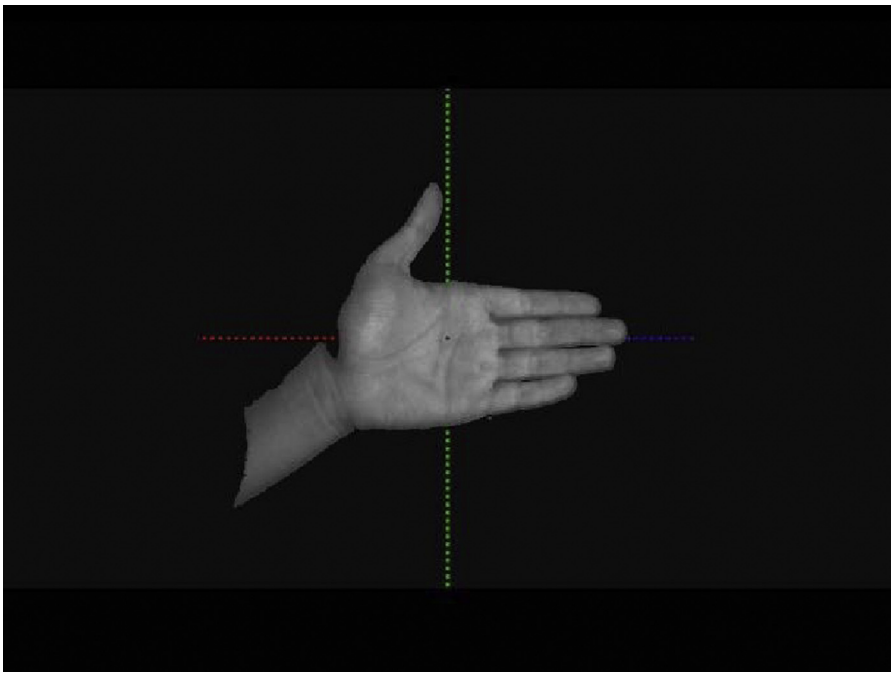

Video S1. A video clip is available online. Supplementary material related to this article can be found online at http://dx.doi.org/10.1016/j.optcom.2014.04.067.

Based on the results above, it is plain to see that the proposed method with considering the lens distortion can effectively reduce the measurement error and greatly improve the accuracy for both in-plane and out-of-plane coordinates.

5.3. *Real-time dynamic scene measurements*

To evaluate the real-time performance of the proposed method, four threads were created for data processing, one was designed for capturing input image, one for phase retrieval and 3-D reconstruction, and the remaining two for 3-D display and invalid pixel elimination [17]. Also, by Eqs. (26), (29)–(32) and (18) (some of them are in the Appendix), LUTs and mapping relationship for distortion correction were pre-calculated and stored.

Firstly a moving human hand was measured and a video is presented (Media 1 [18]). A selected image of the measurement result is shown in Fig. 12(a) where the axes of X_w, Y_w and Z_w were marked with red, green and blue respectively. In the video, we can see that the movements and changes of gestures are very smooth and the hand surface has been well reconstructed. Besides, when the hand is moving back and forth, few distinct invalid points on the edges of the hand can be observed. For comparison, we

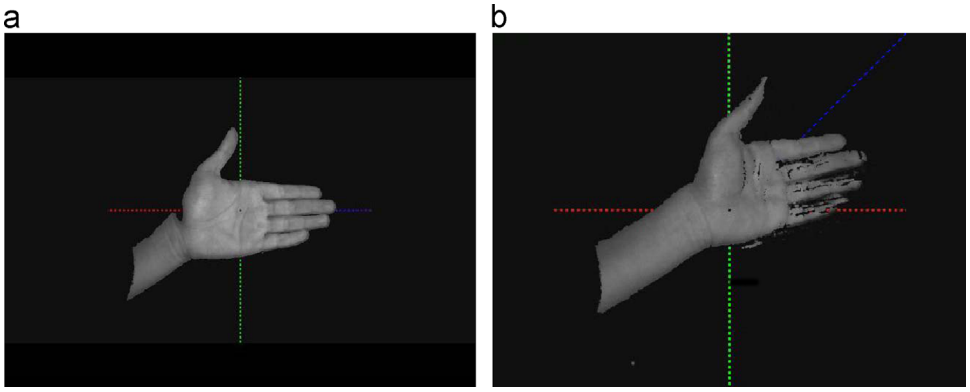

Fig. 12. Real-time measurement results of a moving hand. (a) The 3-D reconstruction result of the proposed method (Media 1) and (b) the 3-D reconstruction of the method without data pre-processing (Media 2).

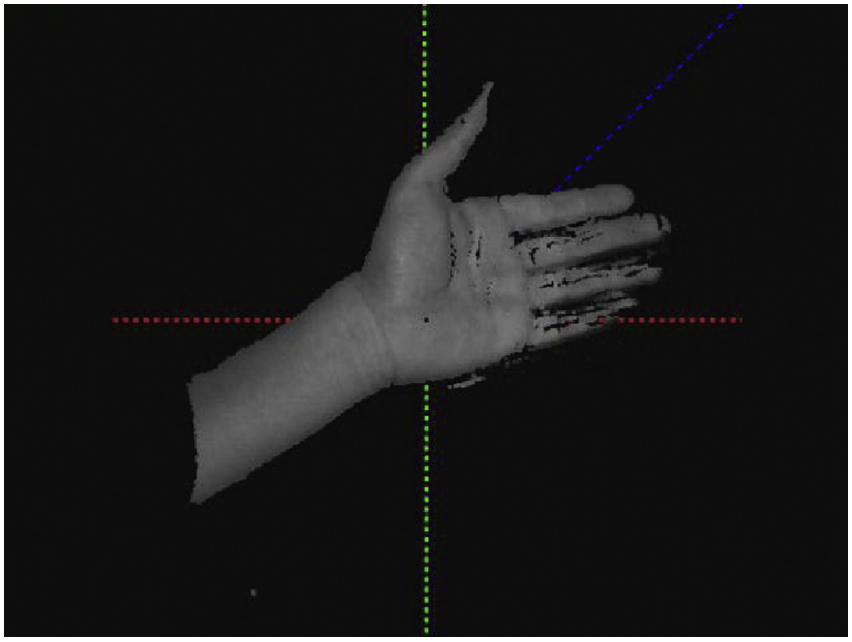

Video S2. A video clip is available online. Supplementary material related to this article can be found online at http://dx.doi.org/10.1016/j.optcom.2014.04.067.

Table 2
The time cost in the real-time measurement.

	Method without data pre-processing	Proposed method
Image distortion correction	47.32	3.25
Phase retrieval	84.49	1.43
Invalid point elimination	1.52	1.53
3-D coordinates calculation	53.67	4.62
Total (*ms*)	186.94	10.83

conducted another experiment without using the LUTs-based processing, and the pixel mapping relation was calculated directly using Eq. (18). The result is shown in Fig. 12(b), and the corresponding video is presented as Media 2 [19], from which the movements of the hand are stumbling and very unsmooth, and large amounts of invalid points arise at the edges of the hand contour when the hand is moving. Finally for quantitative analysis, the average time cost over 800 runs of the two methods is reported in Table 2. With the help of LUTs and the strategy of pre-computing distortion mapping relation, the computational time of the image distortion correction, phase retrieval and 3-D coordinates calculation has been significantly reduced. Furthermore, the total time cost of the proposed method is 10.83 ms which means that as long as the projection and capturing speed are fast enough, a 3-D reconstruction can be acquired at 92.34 frames per second.

Further we measured a more complex scene with multiple objects involving a moving human hand, a static gauge block and a calibration board. The result observed from different views is shown Fig. 13 and a video (Media 3 [20]) is presented, in which the hand still moves smoothly and the profiles of all the three isolated objects have been retrieved correctly.

6. Conclusion

This paper presents a high-speed real-time 3-D coordinates measurement system using fringe projection approach. Only five fringe images are used to obtain the absolute phase map. Using the method of governing equation, the out-plane height is solved firstly, and with the calibrated camera parameters the two corresponding in-plane coordinates are calculated successively. The camera lens distortion is taken into account for improving the 3-D geometric shape measurement accuracy. Compared with the

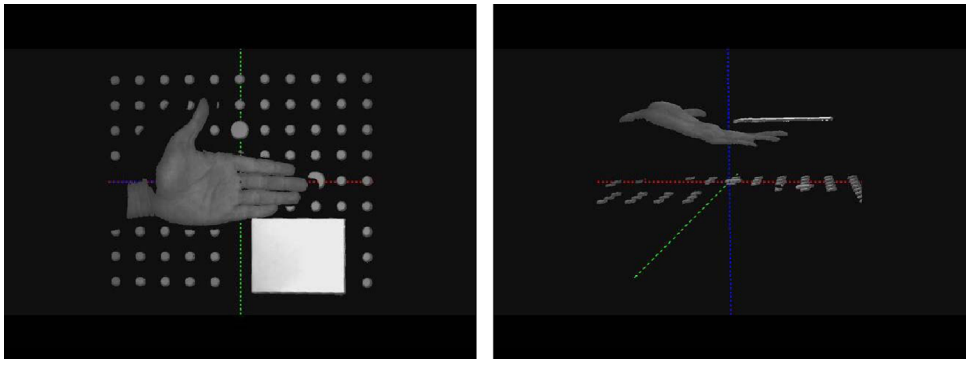

Fig. 13. The real-time measurement result of multiple objects (Media 3).

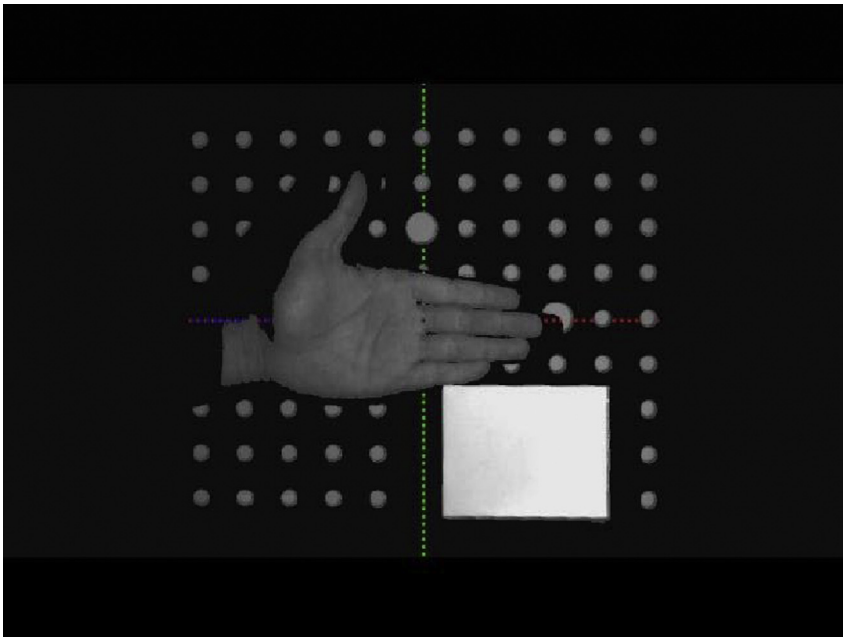

Video S3. A video clip is available online. Supplementary material related to this article can be found online at http://dx.doi.org/10.1016/j.optcom.2014.04.067.

method without considering the lens distortion, the measurement error of in-plane coordinates has been significantly reduced by one order of magnitude by the proposed approach. And with regard to the out-plane height measurement, the RMS is also reduced by two thirds. In addition, owing to the established LUTs for phase retrieval and 3-D coordinates calculation, and the pre-determined pixel mapping relationship for distortion correction, a 3-D reconstruction rate of 92.34 frames per second is achieved.

Acknowledgments

This work was supported by the Research Fund for the Doctoral Program of Ministry of Education of People's Republic of China (No. 20123219110016) and the National Natural Science Foundation of China (No. 61271332), and the Research and Innovation Plan for Graduate Students of Jiangsu Higher Education Institutions, China (No. CXLX13_177).

Appendix

The $X1\_LUT$, $X2\_LUT$, $Y1\_LUT$ and $Y2\_LUT$ can be created as

$$X1\_LUT[u,v]=\frac{bx[u,v]cx[u,v]-ex[u,v]fx[u,v]}{gx[u,v]hx[u,v]-ix[u,v]jx[u,v]}, \tag{29}$$

$$X2\_LUT[u,v]=\frac{ax[u,v]cx[u,v]-dx[u,v]fx[u,v]}{gx[u,v]hx[u,v]-ix[u,v]jx[u,v]}, \tag{30}$$

$$Y1\_LUT[u,v]=\frac{by[u,v]cy[u,v]-ey[u,v]fy[u,v]}{gy[u,v]hy[u,v]-iy[u,v]jy[u,v]},, \tag{31}$$

$$Y2\_LUT[u,v]=\frac{ay[u,v]cy[u,v]-dy[u,v]fy[u,v]}{gy[u,v]hy[u,v]-iy[u,v]jy[u,v]}, \tag{32}$$

where

$$ax[u,v]=x_d r_{33}-r_{13},\quad ay[u,v]=ax[u,v],$$

$$bx[u,v]=x_d t_3-t_1,\quad by[u,v]=bx[u,v],$$

$$cx[u,v]=r_{22}-r_{32}y_n,\quad cy[u,v]=r_{21}-r_{31}y_n,$$

$$dx[u,v]=y_d r_{33}-r_{23},\quad dy[u,v]=dx[u,v],$$

$$ex[u,v]=y_d t_3-t_2,\quad ey[u,v]=ex[u,v],$$

$$fx[u,v]=r_{12}-r_{32}x_n,\quad fy[u,v]=r_{11}-r_{31}x_n,$$

$$gx[u,v]=r_{11}-r_{31}x_n,\quad gy[u,v]=r_{12}-r_{32}x_n,$$

$$hx[u,v]=r_{22}-r_{32}y_n,\quad hy[u,v]=r_{21}-r_{31}y_n,$$

$$ix[u,v]=r_{21}-r_{31}y_n,\quad iy[u,v]=r_{22}-r_{32}y_n,$$

$$jx[u,v] = r_{12} - r_{32}x_n, \quad jy[u,v] = r_{11} - r_{31}x_n,$$

And x_n, y_n can be solved by

$$x_n = \frac{u-u_0}{f_u} \quad and \quad y_n = \frac{v-v_0}{f_v}.$$

References

[1] F. Chen, G.M. Brown, M. Song, Opt. Eng. 39 (2000) 13.
[2] M. Takeda, K. Mutoh, Appl. Opt. 22 (1983) 6.
[3] T.P. Koninckx, L.V. Gool, IEEE. Trans. Pattern. Anal. Mach. Intell. 28 (2006) 14.
[4] Q. Zhang, X. Su, Opt. Express 13 (2005) 7.
[5] S. Zhang, S.-T. Yau, Opt. Eng. 46 (2007) 6.
[6] P.S. Huang, S. Zhang, Appl. Opt. 45 (2006) 6.
[7] V. Srinivasan, H.C. Liu, M. Halioua, Appl. Opt. 23 (1984) 4.
[8] S. Zhang, D. Royer, S.-T. Yau, Opt. Express 14 (2006) 10.
[9] K. Liu, Yongchang Wang, D.L. Lau, Q. Hao, L.G. Hassebrook, Opt. Express 18 (2010) 16.
[10] C. Zuo, Q. Chen, G. Gu, S. Feng, F. Feng, Opt. Express 20 (2012) 18.
[11] C. Zuo, Q. Chen, G. Gu, S. Feng, F. Feng, R. Li, G. Shen, Opt. Lasers Eng. 51 (2013) 8.
[12] Z. Wang, D.A. Nguyen, J.C. Barnes, Opt. Lasers Eng. 48 (2010) 8.
[13] J. Li, L.G. Hassebrook, C. Guan, J. Opt. Soc. Am. A 20 (2003) 10.
[14] S. Zhang, Opt. Eng. 48 (2009).
[15] J. Weng, P. Cohen, M. Herniou, Trans. Pattern Anal. Mach. Intell. 14 (2002) 16.
[16] J.Y. Bouguet, Camera Calibration Toolbox for Matlab.
[17] S. Feng, Q. Chen, C. Zuo, R. Li, G. Shen, F. Feng, Opt. Eng. 52 (2013) 10.
[18] Media 1 ⟨http://www.zuochao.org/uploads/videos/2014_oc_rtcali/Media_1.avi⟩.
[19] Media 2 ⟨http://www.zuochao.org/uploads/videos/2014_oc_rtcali/Media_2.avi⟩.
[20] Media 3 ⟨http://www.zuochao.org/uploads/videos/2014_oc_rtcali/Media_3.avi⟩.